# Relative stopping power resolution in time-of-flight proton CT

Nils Krah, Denis Dauvergne, Jean Michel Létang, Simon Rit, Etienne Testa

# Relative stopping power resolution in time-of-flight proton CT

Nils Krah[1,2], Denis Dauvergne[3], Jean Michel Létang[1], Simon Rit[1], Étienne Testa[2]

[1]University of Lyon, CREATIS, CNRS UMR5220, Inserm U1044, INSA-Lyon, Université Lyon 1, Centre Léon Bérard, France

[2]University of Lyon, Université Claude Bernard Lyon 1, CNRS/IN2P3, IP2I Lyon, UMR 5822, Villeurbanne, France

[3]Université Grenoble Alpes, CNRS/IN2P3, Grenoble INP, LPSC-UMR 5821, Grenoble, France

*nils.krah@creatis.insa-lyon.fr*

**Abstract**

**Objective** Proton computed tomography (CT) is similar to x-ray CT but relies on protons rather than photons to form an image. In its most common operation mode, the measured quantity is the amount of energy that a proton has lost while traversing the imaged object from which a relative stopping power map can be obtained via tomographic reconstruction. To this end, a calorimeter which measures the energy deposited by protons downstream of the scanned object has been studied or implemented as energy detector in several proton CT prototypes. An alternative method is to measure the proton's residual velocity and thus its kinetic energy via the time of flight (TOF) between at least two sensor planes. In this work, we study the RSP resolution, seen as image noise, which can be expected from TOF proton CT systems.

**Approach** We rely on physics models on the one hand and statistical models of the relevant uncertainties on the other to derive closed form expressions for the noise in projection images. The TOF measurement error scales with the distance between the TOF sensor planes and is reported as velocity error in ps/m. We use variance reconstruction to obtain noise maps of a water cylinder phantom given the scanner characteristics and additionally reconstruct noise maps for a calorimeter-based proton CT system as reference. We use Monte Carlo simulations to verify our model and to estimate the noise due to multiple Coulomb scattering inside the object. We also provide a comparison of TOF helium and proton CT.

**Main results** We find that TOF proton CT with 30 ps/m velocity error reaches similar image noise as a calorimeter-based proton CT system with 1% energy error (1 sigma error). A TOF proton CT system with a 50 ps/m velocity error produces slightly less noise than a 2% calorimeter system. Noise in a reconstructed TOF proton CT image is spatially inhomogeneous with a marked increase towards the object periphery. Our modelled noise was consistent with Monte Carlo simulated images. TOF helium CT offers lower RSP noise at equal fluence, but is less advantageous at equal imaging dose.

**Significance** This systematic study of image noise in TOF proton CT can serve as a guide for future developments of this alternative solution for estimating the residual energy of protons and helium ions after the scanned object.

This is a peer-reviewed, un-copyedited version of an article accepted for publication/published in Physics in Medicine and Biology. IOP Publishing Ltd is not responsible for any errors or omissions in this version of the manuscript or any version derived from it. The Version of Record is available online at https://doi.org/10.1088/1361-6560/ac7191.

# 1 Introduction

Proton computed tomography (CT) is a transmission imaging modality similar to x-ray CT which uses protons instead of x-ray for image acquisition (Johnson, 2018). While x-ray CT relies on attenuation, proton CT is typically operated in energy-loss mode where the amount of energy lost by a proton while traversing the imaged object depends on the water equivalent amount of material. The reconstructed quantity in this case is the so-called relative stopping power (RSP), i.e. the proton stopping power relative to that of water. A proton CT scanner typically includes a suitable detector to measure the protons' residual energy, i.e. after traversing the scanned object, from which, together with the beam energy, the energy loss can be obtained. Proton CT scanner prototypes proposed and developed so far rely either on a calorimeter, e.g. a scintillator, to measure the energy deposited by a proton therein (Civinini et al., 2013; Johnson et al., 2016; DeJongh et al., 2021) or a range telescope (Taylor et al., 2016; Alme et al., 2020; Pemler et al., 1999). An alternative measurement principle determines the proton's time of flight (TOF) between two or more sensor planes from which the velocity and thus the kinetic energy can be calculated. Although Worstell et al. (2019) reported on developments of a TOF proton radiography system and presented some first experimental results, TOF proton CT has overall not been fully explored yet. Ulrich-Pur et al. (2022) recently investigated the feasibility of a TOF proton CT system using low gain avalanche detectors (Pellegrini et al., 2014) based on Monte Carlo simulations. They studied RSP accuracy and RSP resolution with a focus on the detector hardware and possible calibration procedures. Volz (2020) discusses TOF as an alternative measurement principle in helium CT and analyses aspects related to RSP resolution. RSP resolution has previously been investigated for energy-loss proton CT based on calorimeter detectors (Schulte et al., 2005; Collins-Fekete et al., 2021; Rädler et al., 2018; Dickmann et al., 2019) as well as for other proton CT modalities which do not require residual energy measurements (Quiñones et al., 2016; Krah et al., 2020).

This work provides a concise and systematic study of RSP resolution in TOF proton CT, which manifests itself as image noise, based on physics models and statistics. As sources of uncertainty, we consider the TOF measurement error, energy straggling inside the imaged object, as well as the proton beam's energy spread. We analyse noise on a projection level and also reconstruct RSP noise images (Wunderlich et al., 2008; Rädler et al., 2018) of a water cylinder to assess the RSP noise depending on the location in the reconstructed image. In this context, we consider only direct reconstruction algorithms (Khellaf et al., 2020) and distance driven binning backprojection in particular (Rit et al., 2013). We perform Monte Carlo simulations to verify our noise model and reconstruction and to estimate the image noise due to multiple Coulomb scattering inside the object. Finally, we derive all relevant expressions for TOF helium CT in relation to TOF proton CT (in the annex and the discussion), at equal residual range, and compare the RSP resolution that can be achieved with the two ion species.

The contribution of this work is to provide the necessary tools to quickly model RSP resolution in a TOF proton CT system and to derive figures of merit of the achievable RSP resolution given the system's characteristics and the properties of the imaged object, similar to the pioneering work of Schulte et al. (2005) for energy-loss proton CT.

# 2 Materials and Methods

## 2.1 Statistical aspects of TOF proton CT

With *RSP noise* in the proton CT images, we intend the square root of the variance of an RSP value which one would observe in each pixel in repeated acquisitions of the same object, as described e.g. in (Wunderlich et al., 2008). We use *RSP noise* and *RSP resolution* as synonyms. The RSP value is obtained via tomographic image reconstruction which takes a series of projections as input. The projections contain water equivalent path length (WEPL) values

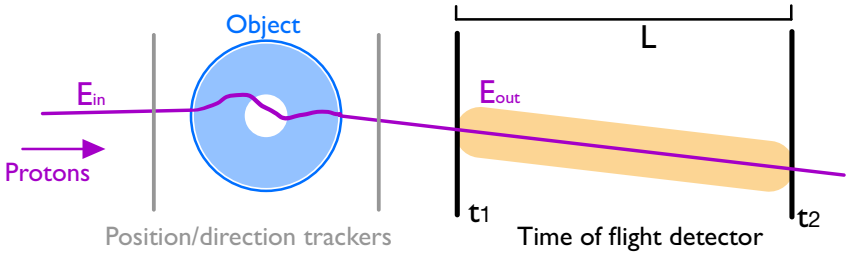


Figure 1: Schematic illustration of a TOF proton CT scanner. The residual energy is deduced from the time $t_2 - t_1$ which the proton needs to travel from one sensor plane to the other. The trackers which measure the proton's position and direction are shown for completeness, although not directly relevant for this work.

which are in turn converted from the proton's energy-loss, e.g. via a look-up table. Therefore, statistical errors in the energy-loss are propagated into the reconstructed RSP value.

We consider a TOF proton CT set-up made of a TOF device consisting of two sensor planes downstream of the scanned object. A proton CT scanner typically also includes tracking devices upstream and downstream of the scanned object, but they are not directly relevant to this work. A sketch is shown in figure 1. We assume that the TOF device records the time needed to travel from one sensor plane to the other, from which the proton's kinetic energy downstream of the imaged object can be determined. The initial proton energy is taken as the beam energy provided by the accelerator. We do not attempt to simulate any specific TOF proton CT prototype.

We consider three contributions to image noise, namely the error of the TOF measurement, energy straggling experienced by the protons, and the energy spread of the proton beam. We denote with $E_{\text{in}}$ and $E_{\text{out}}$ the proton's energy upstream and downstream of the imaged object, respectively. We disregard nuclear interactions and assume that protons recorded by the proton CT system have only undergone electromagnetic interactions. In practice, most protons which have undergone nuclear interactions are filtered out from the data prior to image reconstruction (Johnson, 2018; Schulte et al., 2008). We treat energy straggling and the time measurement error of the TOF device within the Gaussian approximation.

$E_{\text{out}}$ is determined from the time of flight between the TOF sensor planes, $t_2 - t_1$, as

$$E_{\text{out}} = \frac{m_p c^2}{\sqrt{1-(v/c)^2}} - m_p c^2 \quad \text{with} \quad v = \frac{L}{t_2 - t_1}, \tag{1}$$

where $L$ is the distance between the TOF sensor planes and $m_p = 938\,\text{MeV/c}^2$ is the proton mass. Energy loss in 1 mm of silicon or 1 m of air is on the order of 0.5 MeV for protons with an energy between 100 MeV and 200 MeV (Berger et al., 2005). We therefore neglect energy loss in the trackers, the TOF sensors, and the surrounding air. By first order error propagation one has

$$\sigma_{E_{\text{out}},\text{TOF}}(E_{\text{out}}) = \left( \left|\frac{\mathrm{d}E}{\mathrm{d}t_1}\right|^2 \sigma_{t_1}^2 + \left|\frac{\mathrm{d}E}{\mathrm{d}t_2}\right|^2 \sigma_{t_2}^2 \right)^{1/2} = \frac{1}{m_p^2 c^3} (E_{\text{out}}^2 + 2 m_p c^2 E_{\text{out}})^{3/2} \, \frac{\sigma_t}{L}, \tag{2}$$

where $\sigma_t^2 = \sigma_{t_1}^2 + \sigma_{t_2}^2$ is the TOF measurement error stemming from the time resolution of the two sensors. Note that the error on $E_{\text{out}}$ directly scales with $L$ so that a greater spacing between the TOF planes will reduce the energy measurement error. Throughout this work, we report the velocity error $\sigma_t/L$ in units of ps/m, rather than $\sigma_t$ alone.

Energy straggling of protons inside the imaged object and detectors leads to a variation of $E_{\text{out}}$ and acts as another source of statistical error in the data (Schulte et al., 2005). The energy spread due to straggling can be modelled theoretically via partial differential equations (Tschalär, 1968) and solved analytically (Payne, 1969), yielding

$$\sigma^2_{E_{\text{out}},\text{straggling}}(E_{\text{out}}) = \chi_1^2(E_{\text{out}}) \int_{E_{\text{out}}}^{E_{\text{in}}} \frac{\chi_2(E)}{\chi_1^3(E)}\,\mathrm{d}E, \tag{3}$$

where $\chi_1(E)$ and $\chi_2(E)$ are defined as follows:

$$\chi_1(E) = K\frac{1}{\beta^2}\left[\ln\left(\frac{2m_e c^2\beta^2}{I(1-\beta^2)}\right) - \beta^2\right] \tag{4}$$

$$\chi_2(E) = Km_e c^2 \frac{1-\beta^2/2}{1-\beta^2} \quad \text{with} \quad \beta = \frac{v}{c} = \left[1 - \left(\frac{m_p c^2}{m_p c^2 + E}\right)^2\right]^{1/2}. \tag{5}$$

Here, $I$ is the ionisation potential of the target material of interest which we approximate to be water ($I$=75 eV, Berger et al. (1993)), $m_e$ and $m_p$ are the electron and proton masses, respectively, $\beta$ the proton velocity relative to the speed of light, and $K = 170\,\text{keV/cm}$ is a constant. Note that $\chi_1(E)$ is identical to the stopping power given by the Bethe-Bloch equation (Paganetti, 2012). We solved equation 3 numerically.

Because the protons' energy loss, $\Delta E = E_{\text{out}} - E_{\text{in}}$, is obtained as the difference between the measured exit energy and the incident energy determined from the beam energy provided by the proton accelerator, the energy spread of the incident beam (standard deviation $\sigma_{\text{beam}}$; hereafter denoted as beam spread) acts as an additional error. As a figure of merit, the relative energy spread of a therapeutic proton beam, $\delta E_{\text{beam}} = \sigma_{\text{beam}}(E_{\text{in}})/E_{\text{in}}$ is typically 0.5% to 1% of the beam energy (Schippers, 2018). The overall error in the energy loss is the squared sum of the contributions due to straggling, TOF measurement error, and beam spread, i.e.

$$\sigma^2_{\Delta E}(E_{\text{out}}) = \sigma^2_{E_{\text{out}},\text{straggling}}(E_{\text{out}}) + \sigma^2_{E_{\text{out}},\text{TOF}}(E_{\text{out}}) + (\delta E_{\text{beam}} E_{\text{in}})^2. \tag{6}$$

Note that our model disregards the noise induced by multiple Coulomb scattering on target nuclei in the scanned object (Dickmann et al., 2019). The reason is that it depends on the shape and composition of the object and is therefore not purely characteristic of the TOF proton CT scanner. We estimated the noise contribution due to multiple Coulomb scattering via Monte Carlo simulation (see section 2.5).

In distance driven proton CT reconstruction (Rit et al., 2013), the WEPL value in a pixel is obtained by converting energy loss to WEPL and averaging the WEPL of all protons binned in that pixel. The relation between WEPL and exit energy $E_{\text{out}}$ is analytically given by

$$\text{WEPL}(E_{\text{out}}) = \int_{E_{\text{in}}}^{E_{\text{out}}} 1/S_w(E)\,\mathrm{d}E. \tag{7}$$

In this work, we performed the integration in equation 7 numerically using the stopping power $S_w(E)$ of water from NIST's PSTAR table (Berger et al., 2005). We obtained the conversion from WEPL to $E_{\text{out}}$ by numerical inversion. The energy error propagates (first order) to an error of the WEPL value averaged over $N$ protons, $\sigma_{\text{WEPL}}$, as

$$\sigma^2_{\text{WEPL}}(E_{\text{out}}) = \frac{\sigma^2_{\Delta E}(E_{\text{out}})}{S_w^2(E_{\text{out}})N} = \frac{\sigma^2_{\Delta E}(E_{\text{out}})}{S_w^2(E_{\text{out}})\Phi\Delta\xi^2}, \tag{8}$$

where $S_w(E_{\text{out}})$ is the proton stopping power in water at the energy $E_{\text{out}}$. The number of protons $N$ contributing to a given pixel has been re-expressed as the product of fluence $\Phi$ and area of reference, in this case the pixel area $\Delta\xi^2$. Equation 8 above combines contributions to WEPL error due to straggling, measurement error, and beam spread.

We also consider a proton CT system using a calorimeter as energy detector, e.g. a scintillator coupled with photo multipliers (Johnson et al., 2016). Bashkirov et al. (2016) parametrise the measurement uncertainty via a constant relative error, $\delta E_{\text{out,cal}} \equiv \sigma_{E_{\text{out,cal}}}/E_{\text{out}}$ on the order of a few percent. The $\sigma^2_{E_{\text{out}},\text{TOF}}$ term in equation 6 is replaced by $(\delta E_{\text{out,cal}} E_{\text{out}})^2$ in this case.

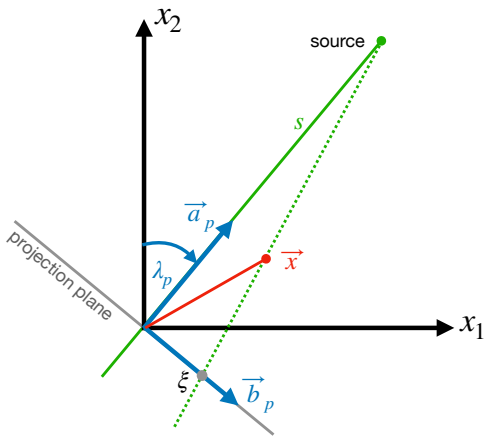


Figure 2: Scanner geometry considered in the noise reconstructions.

## 2.2 Noise reconstructions

In statistical terms, the noise in the reconstructed proton CT images is the variance of the reconstructed RSP value in each image pixel. This can be obtained, e.g., by simulating many independent proton CT acquisitions and calculating the voxel-wise root-mean-square-error (RMSE) over the ensemble of reconstructed images. However, it is also possible to reconstruct noise images (Wunderlich et al., 2008) starting from noise projections. Rädler et al. (2018) have implemented this method for proton CT. We implemented the noise reconstruction using a cone beam geometry and a full circular ($2\pi$) acquisition trajectory with radius $R_0$, but we only reconstructed the central slice. For the purpose of this work, we therefore limit our geometry to a two-dimensional description. We briefly describe our noise reconstruction in the following and refer to Wunderlich et al. (2008) and Rädler et al. (2018) for a detailed description of the underlying considerations.

An illustration of the geometry is shown in figure 2. We place the rotation axis at the origin $(0, 0)$. The source angle is denoted with $\lambda_p$ and increases clockwise, $s$ is the source to centre distance, and $\vec{a}_{\lambda_p}$ is the source position in two dimensional Cartesian coordinates, i.e. $\vec{a}_{\lambda_p} = s(\sin\lambda_p, \cos\lambda_p)^T$. The basis vector of the projection plane (1D) going through $(0, 0)$ is $\vec{b}_{\lambda_p} = (\cos\lambda_p, -\sin\lambda_p)^T$ and $\xi$ refers to the coordinate in the projection frame. For a given point $\vec{x} = (x_1, x_2)^T$ and source angle $\lambda_p$, the coordinate $\xi$ in the projection frame is given by

$$\xi = \vec{x} \cdot \vec{b}_{\lambda_p} \frac{s}{s - \vec{x} \cdot \vec{a}_{\lambda_p}} = \frac{s\,(x_1 \cos\lambda_p - x_2 \sin\lambda_p)}{s - x_1 \sin\lambda_p - x_2 \cos\lambda_p}. \tag{9}$$

The position $\xi$ and the angle $\lambda_p$ are sampled uniformly, i.e.

$$\lambda_p = (p-1)\Delta\lambda, \quad p = 1, 2, \ldots, P \tag{10}$$

$$\xi_j = (j + 1/2)\Delta\xi, \quad j = -J, -J+1, \ldots, J-1 \tag{11}$$

with $\Delta\lambda$ the angular spacing between projections, $P$ the number of projections, $\Delta\xi$ the pixel width in a projection, and $2J$ the number of sampled positions in the central projection plane.

We assumed that projections are filtered with an apodized ramp filter (Ramachandran et al., 1971),

$$h_F(\xi_j) = h_F((j + 1/2)\Delta\xi) = \begin{cases} 1/(2\Delta\xi)^2 & \text{for } j = 0, \\ 0 & \text{for } j \text{ even and } j \neq 0 \\ -1/(j\pi\Delta\xi)^2 & \text{for } j \text{ odd}, \end{cases} \tag{12}$$

and that the central image slice is reconstructed with the Feldkamp-Davis-Kress (FDK) algorithm (Feldkamp et al., 1984), which is the case in the distance driven binning algorithm in (Rit et al., 2013). For simplicity, we treated proton trajectories as straight lines and therefore only used one projection image per projection angle corresponding to the central depth, unlike Rädler et al. (2018) who considered the influence of multiple Coulomb scattering.

In general, the variance of the RSP value at point $\vec{x}$ is calculated by backprojecting the variance and covariance of the filtered projections, where the covariance arises from the combination of interpolation and filtering. We use a simplified version of the noise reconstruction which replaces the covariance term (for bilinear interpolation of projections filtered by the same apodized ramp filter) by an effective factor $f_{\text{interp}} = 2/3 - 2/\pi^2$ (Rädler et al., 2018). This avoids interference patterns in the noise distributions due to correlations among pixels and makes the results easier to interpret. In particular, the RSP variance at $\vec{x}$ is

$$\text{Var}_{\text{RSP}}(\vec{x}) = f_{\text{interp}} \frac{\Delta\lambda^2}{4} \sum_{p=1}^{P} \left( \frac{\|\vec{a}_{\lambda_p}\|}{\|\vec{x} \cdot (\vec{a}_{\lambda_p}/s) - \vec{a}_{\lambda_p}\|} \right)^4 V_p(\xi_k). \tag{13}$$

The term $V_p(\xi_k)$ is the variance in the filtered projections at $\xi_k$,

$$V_p(\xi_k) = (\Delta\xi)^2 \sum_{j=-J}^{J-1} h_F^2(\xi_k - \xi_j) \frac{\|\vec{a}_{\lambda_p}\|^2}{\|\vec{a}_{\lambda_p}\|^2 + \xi_j^2} \text{Var}(\lambda_n, \xi_j), \tag{14}$$

where $\text{Var}(\lambda_n, \xi_j)$ refers to the noise projection containing the WEPL variance (equation 8), $\frac{\|\vec{a}_{\lambda_p}\|^2}{\|\vec{a}_{\lambda_p}\|^2 + \xi_j^2}$ is a weighting factor (A. Kak et al., 2001). Equations 13 and 14 were adapted from (Rädler et al., 2018) to consider a divergent beam geometry.

## 2.3 Simulations and phantoms

In the following, we describe how we simulated noise projections which then served as input to the reconstructions described in section 2.2. The simulations steps included forward projections which we performed along straight lines for simplicity, i.e. we approximated proton paths as straight lines thereby neglecting the effect of multiple Coulomb scattering in the projection operation. This simplified the noise reconstruction because distance-driven binning was not necessary. We consider the influence of multiple Coulomb scattering on RSP noise via Monte Carlo simulation (see section 2.5).

We used a cylindric water phantom with a 20 cm diameter and with infinite axial extension. To simulate noise projections, we forward projected RSP values of the phantom to obtain a projection image containing WEPL values, converted these into energy loss via the inverse of equation 7, and calculated the variance projections $\text{Var}(\lambda_n, \xi_j)$ via equation 8 as described in section 2.1. Energy loss and scattering in the air were neglected, given that 1 m of air corresponds to only 1 mm of water in terms of mass density. We used 360 projection angles uniformly distributed over a full circular trajectory and assumed a source-to-center distance of 200 cm, which is representative of many modern therapeutic proton accelerators. The pixel size was $1 \times 1\,\text{mm}^2$, both in the projection images and in the reconstructed images. We considered an energy spread of the proton beam of $\delta E_{\text{beam}} = 0.5\%$ as a figure of merit (Schippers, 2018).

We determined the number of protons contributing to a pixel in equation 8 in relation to the dose at the phantom centre of 10 mGy accumulated over an entire proton CT scan. Specifically, the fluence at the exit of the cylinder, $\Phi_{\text{out}}$, i.e. the fluence of protons measurable by the energy detector, depends on the thickness of material traversed by the protons expressed in WEPL, which we denote with $W(\xi)$ and which depends on the location $\xi$ in the projection plane (but not on the angular source position $\lambda_p$ because the scanned object is a cylinder). Assuming a spatially constant initial fluence, $\Phi_{\text{in}}$, one can relate $\Phi_{\text{out}}(W(\xi))$ and the proton fluence at the cylinder centre $\Phi_{\text{centre}}$:

$$\Phi_{\text{out}}(W(\xi)) = \Phi_{\text{in}} \exp(-\kappa W(\xi)) = \Phi_{\text{centre}} \exp(-\kappa(W(\xi) - R)), \tag{15}$$

where $R$ is the cylinder radius and $\kappa = 0.01\,\text{cm}^{-1}$ is a coefficient describing attenuation due to nuclear interactions in water (Schulte et al., 2005; Quiñones et al., 2016). $\Phi_{\text{centre}}$ is related to the dose $D_{\text{centre}}$ accumulated at the cylinder centre during a full pCT scan ($P$ projections) (Schulte et al., 2005):

$$\Phi_{\text{centre}} = \frac{D_{\text{centre}}\rho}{P\left[S(E_{\text{centre}}) + \kappa\gamma E_{\text{centre}}\right]}, \tag{16}$$

where $S(E_{\text{centre}})$ is the proton stopping power for the proton energy at the centre, $\rho$ is the mass density of the cylinder material (in our case water, i.e. $\rho = 1\,\text{g/cm}^3$), $\gamma$=0.65 is the fraction of energy transferred to secondary particles during nuclear interactions (in the energy range up to 200 MeV, in water-like material). In a water cylinder with $R = 10\,\text{cm}$ radius and for a 200 MeV proton beam, one has $E_{\text{centre}} \approx 151\,\text{MeV}$ and consequently a proton stopping power $S(E_{\text{centre}})$ in water of about $5.4\,\text{MeV cm}^2/\text{g}$ (Berger et al., 2005). With these numbers, equation 16 yields a fluence at the centre of 270 protons per $\text{mm}^2$ per projection, which corresponds well to the numbers in Schulte et al. (2005) estimated via Geant4 Monte Carlo simulation (Agostinelli et al., 2003).

The full expression for the modelled variance projection is obtained by combining equations 8, 15, and 16,

$$\text{Var}(\lambda_p, \xi_j) = \frac{\sigma^2_{E_{\text{out}}}(\lambda_p, \xi_j)}{S^2_w(E_{\text{out}}(\lambda_p, \xi_j))} \frac{P\left[S(E_{\text{centre}}) + \kappa\gamma E_{\text{centre}}\right]}{D_{\text{centre}}\rho\Delta\xi^2} \exp\left(\kappa\left(W(\lambda_p, \xi_j) - R\right)\right), \tag{17}$$

where $W(\lambda_p, \xi_j)$ is the WEPL at sampling point $\xi_j$ in projection $\lambda_p$ and $E_{\text{out}}(\lambda_p, \xi_j)$ is obtained from $W(\lambda_p, \xi_j)$ via the inverse of equation 7.

## 2.4 Monte Carlo simulations

To verify our noise reconstructions, we performed Geant4/Gate Monte Carlo simulations (Agostinelli et al., 2003; Sarrut et al., 2014) of a TOF proton CT scan of the water cylinder. The simulation set-up was the same as in (Quiñones et al., 2016). Specifically, we used a 200 MeV incident proton beam with a 1 MeV energy spread in a fan beam geometry and a source-to-isocentre distance of 1 m. Each proton's position and direction was recorded in a plane upstream and downstream of the scanned object, to mimic the trackers (see figure 1). The residual energy was recorded in the downstream tracker plane and an uncertainty corresponding to a certain TOF velocity error was added in a post-processing step. We used the *QGSP_BIC* physics list which includes nuclear interactions and thus the effect of nuclear attenuation, but we filtered out all protons in a post processing step which had undergone nuclear interactions. Per scan, we simulated 360 projections in 1 degree intervals. Images (the central slice at $z = 0$) were reconstructed via distance driven binning (Rit et al., 2013) using a pixel size of $1\,\text{mm}^2$. We simulated and reconstructed a total of 100 images and calculated the pixel-wise root mean square error as a direct estimate of the RSP noise.

## 2.5 Noise due to multiple Coulomb scattering

Another source of noise in proton CT images, independent of the energy detection method, is the stochastic nature of the proton trajectories due to multiple Coulomb scattering (Rädler et al., 2018; Dickmann et al., 2019; Collins-Fekete et al., 2021). In particular, protons contributing to the same pixel in the projection plane traverse the object along different (random) trajectories and therefore accumulate different WEPL values depending on the shape and composition of the

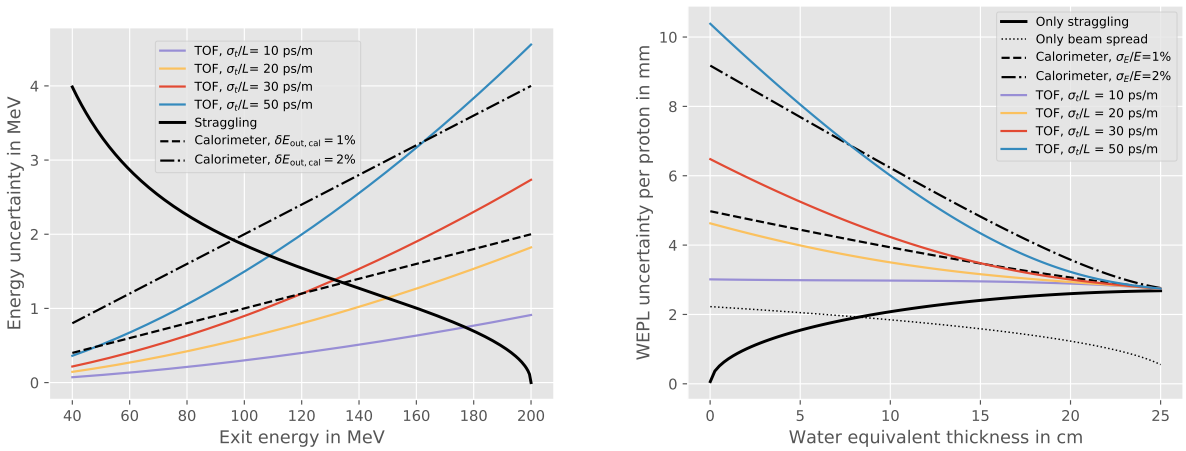


Figure 3: Left: Energy uncertainty (1 sigma) due to straggling and energy measurement error for different velocity errors $\sigma_t/L$ and a beam energy of 200 MeV. The dashed and dash-dotted lines depict a 1% and 2% uncertainty of a calorimeter detector, respectively. Right: WEPL uncertainty (1 sigma) of a proton CT system (equation 8) as a function of WEPL for a beam energy of 200 MeV and different velocity errors $\sigma_t/L$. WEPL uncertainties for a calorimeter-based system (dashed, dash-dotted) are shown for comparison.

object. In this sense, the geometrical uncertainty about the protons' trajectory translates into a WEPL uncertainty. In the water cylinder considered in this work, the WEPL uncertainty only stems from the external shape of the cylinder, while internal density gradients would also play a role in a patient.

We estimated the noise contribution due to multiple Coulomb scattering based on the Monte Carlo simulated data. In particular, we calculated the difference between the RSP variance in the simulated images (see section 2.4), $\mathrm{Var}_{\mathrm{RSP,MC}}$, and the one predicted by our model (equation 13), $\mathrm{Var}_{\mathrm{RSP}}$, i.e.

$$\sigma_{\mathrm{RSP,MCS}} = \sqrt{\mathrm{Var}_{\mathrm{RSP,MC}} - \mathrm{Var}_{\mathrm{RSP}}}. \tag{18}$$

The rationale behind this is that the Monte Carlo simulation includes all sources of RSP uncertainty while our model includes all but multiple Coulomb scattering. A similar approach was used in (Dickmann et al., 2019). Note that $\sigma_{\mathrm{RSP,MCS}}$ is a noisy estimate itself because of the statistical error in the Monte Carlo simulations.

## 3 Results

The left panel in figure 3 shows the energy uncertainty due to the energy measurement error, either via TOF (solid) or via calorimeter (dashed, dash-dotted), and due to straggling (solid black) for an incident beam energy of 200 MeV. Throughout the results section, we report all uncertainties as one sigma errors, i.e. one standard deviation. It is intuitively clear that the energy uncertainty due to TOF error decreases with decreasing exit energy because the lower the proton's energy, the longer its time-of-flight so that the time resolution of the TOF sensors has less impact on the estimated velocity. The limit is that protons still need to reliably traverse the scanned object rather than lose all their energy inside. The lowest depicted energy value of 40 MeV corresponds to a residual range of about 1.5 cm. Straggling, on the other hand, increases with the degree to which a proton has been slowed down due to electromagnetic interactions and thus increases with decreasing exit energy.

The right panel in figure 3 shows how the combined energy uncertainty (due to straggling,

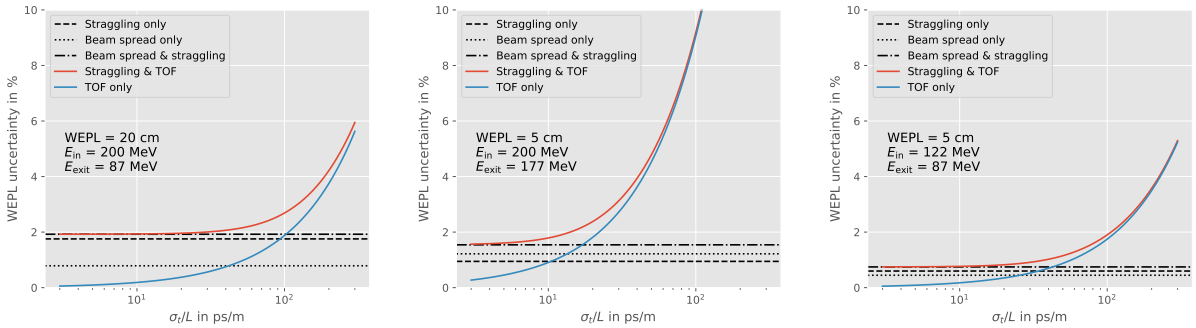


Figure 4: WEPL uncertainty in a TOF proton CT as a function of velocity error $\sigma_t/L$ for three different combinations of object thickness and beam energy.

measurement error, and beam spread) translates into WEPL uncertainty as a function of the phantom's water equivalent thickness, again for a beam energy of 200 MeV. In thin objects, it is mainly the TOF error which dominates the WEPL uncertainty while it is mainly straggling in thicker objects. For velocity errors larger than 50 ps/m, the measurement error is more dominant than straggling for almost all WEPLs. Overall, the WEPL uncertainty of a 20-30 ps/m TOF proton CT system is comparable to a calorimeter-based system with 1% energy measurement error, while a 2% calorimeter error corresponds to a velocity error $\sigma_t/L$ of about 50 ps/m. Note that the WEPL error due to the incident energy spread decreases with increasing WEPL because it depends inversely on the stopping power S (equation 8).

Figure 4 compares the three contributions to WEPL uncertainty, i.e. straggling, TOF measurement error, and beam spread, as a function of the velocity error $\sigma_t/L$ for an object thickness of 5 cm and 20 cm, as indicated in the plots. With a WEPL of 20 cm, the point of equal contribution (straggling + beam spread = TOF error) is found at $\sigma_t/L$ =100 ps/m. With a WEPL of 5 cm, on the other hand, the TOF error begins to dominate already for $\sigma_t/L \approx 20$ ps/m. Lowering the beam energy to 122 MeV, which corresponds to the same exit energy of 86 MeV as for the 20 cm/200 MeV case, shifts the equal contribution point to about 40 ps/m.

The four upper panels in figure 5 show the RSP noise maps for a water cylinder with 20 cm diameter and different velocity errors $\sigma_t/L$ (TOF system) and $\delta E = \sigma_E/E$ (calorimeter system), as indicated in the graphics. The noise images were simulated as described in section 2.3 and reconstructed according to section 2.2. The two lower panels show radial noise profiles for different values of $\sigma_t/L$, for calorimeter resolutions of $\delta E = 1\%$ and $\delta E = 2\%$, and the idealised case where only straggling and the beam's energy spread contribute to image noise. Noise is distributed quite evenly for $\sigma_t/L$ between 10 and 20 ps/m, while there is a marked increase towards the phantom edge for higher values of $\sigma_t/L$, e.g. by a factor of 1.6 for $\sigma_t/L$=50 ps/m. This is because WEPL uncertainty depends on WEPL (see figure 3) and in locations close to the edge, protons only traverse a thin tangential portion of the phantom under certain projection angles. The backprojection operation in the reconstruction therefore accumulates higher noise over all projections for points near the edge than for points close to the centre. A similar tendency is seen for the calorimeter-based system, where the 1% case yields noise profiles comparable to the 30 ps/m TOF system. At first sight, it seems surprising that the 50 ps/m TOF case yields lower RSP noise than the 2% calorimeter system at all distances from the centre although figure 3 suggests similar performance. This is understandable because even at a location close to the edge within the cylinder, the proton WEPL is relatively large for most projection angles and the TOF system performs better than the calorimeter-based set-up for any WEPL larger than 8 cm (figure 3). With the lower beam energy of 180 MeV, which corresponds to 1.6 cm residual range after 20 cm of water, RSP noise reaches the intrinsic limit imposed by straggling and the beam's energy spread, at least for the inner half of the cylinder.

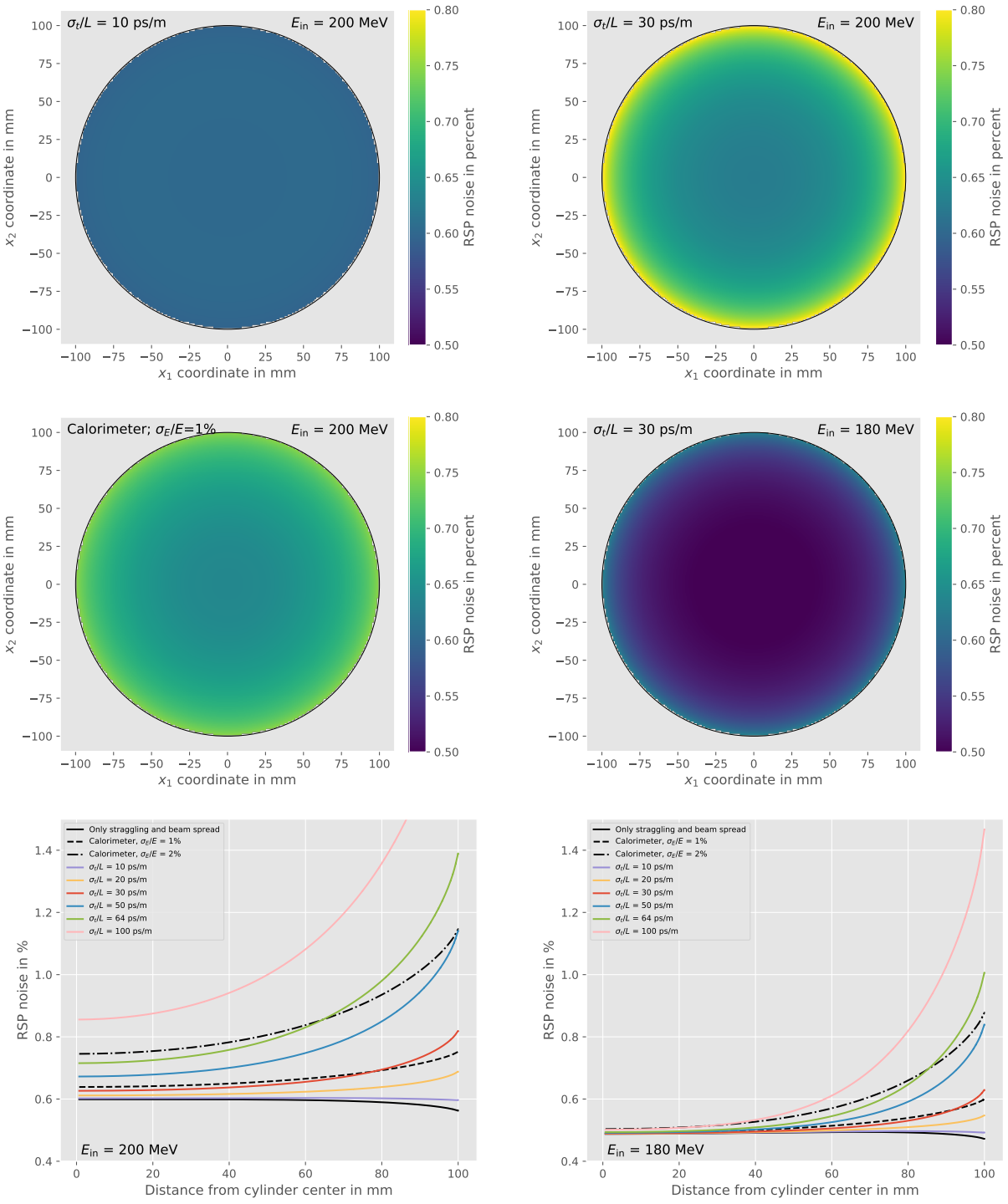


Figure 5: Upper panels: noise reconstructions of a water cylinder of 20 cm diameter for different velocity errors $\sigma_t/L$ and calorimeter measurement errors as well as different incident beam energies as indicated in the graphics. Lower panels: Radial profiles of the RSP noise for 200 MeV (left) and 180 MeV (right) beam energy. Note: The reconstructions shown here do not consider noise due to multiple Coulomb scattering.

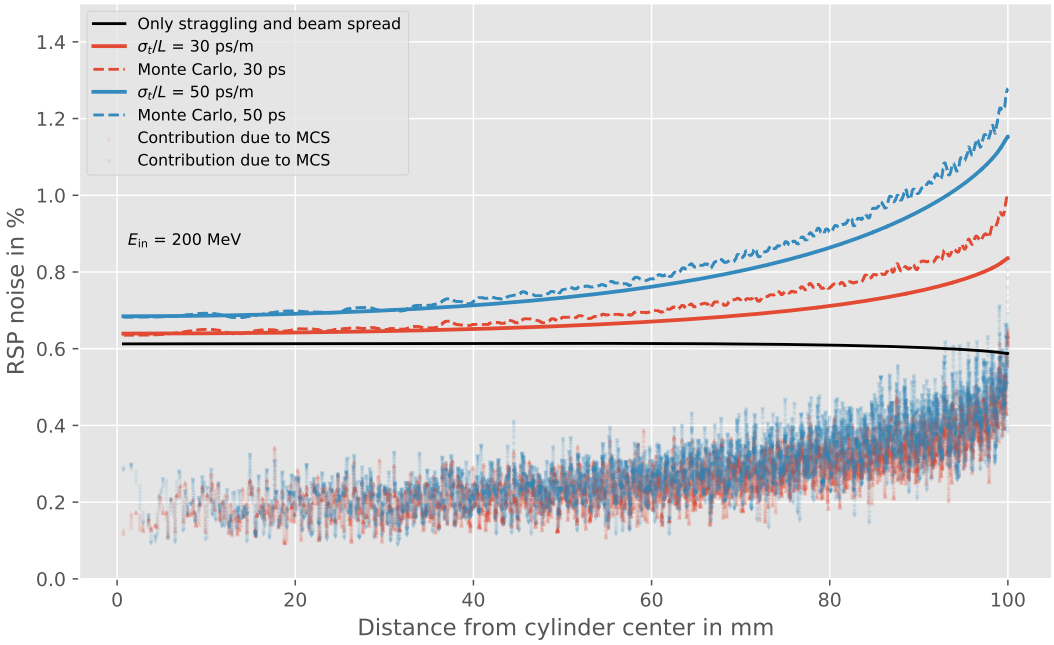


Figure 6: Comparison of RSP noise directly derived from Monte Carlo simulated images (section 2.4) and modelled/reconstructed as presented in this work (sections 2.1 and 2.2). The red and blue scattered data is the noise contribution due to multiple Coulomb scattering estimated as squared difference between Monte Carlo and modelled data (section 2.5).

Figure 6 shows the results of our Monte Carlo simulations (see section 2.4) compared with our model prediction. The modelled RSP noise profiles (red and blue lines) were obtained as noise reconstructions as explained in section 2.2 and are analogous to the lower left panel in figure 5. The noise images were both, simulated and reconstructed, along straight lines. The Monte Carlo simulated data were used to reconstruct 100 independent proton CT images of the water cylinder via distance-driven binning (Rit et al., 2013), i.e. accounting for multiple Coulomb scattering via the most likely path (Schulte et al., 2008). The radial RSP noise profiles calculated as pixel-wise root-mean-square error over the 100 images are presented as red and blue dashed lines. The Monte Carlo simulated RSP noise is in good agreement with the respective modelled noise, but slightly higher because it also contains the contribution due to multiple Coulomb scattering (red and blue triangles). The fact that the estimated multiple Coulomb scattering noise is equal for both velocity errors indicates that our noise model is consistent because multiple Coulomb scattering noise should indeed only depend on the scanned object and the beam parameters, but not on the uncertainty of the residual energy detection.

# 4 Discussion

The purpose of this work was to investigate the RSP noise, i.e. RSP resolution, in time-of-flight proton CT based on physics models and statistics. Our results show that an RSP resolution of better than 1% can be achieved in a water cylinder of 20 cm and a beam energy of 200 MeV, which is representative of a human head and therapeutic proton accelerator, and with a velocity error of a few tens of ps/m. The dose to the phantom centre was 10 mGy. Note that WEPL and thus RSP variance are inversely proportional to the square root of dose (equations 8 and 16) so that lowering the dose by a factor of 10 would increase the RSP noise by a factor of $\sqrt{10} \approx 3.16$. On the other hand, we point out that the RSP variance is inversely proportional to the fourth power of the pixel size, i.e. $\mathrm{Var}_{\mathrm{RSP}}(\vec{x}) \propto \Delta\xi^{-4}$ (equation 13), where a factor of $1/\Delta\xi^2$ results

from the filtering operation (equations 14 and 12) and another factor of $1/\Delta\xi^2$ is linked to the number of protons per pixel (equation 8) (Schulte et al., 2005; Quiñones et al., 2016; Krah et al., 2020). Thus, increasing pixel size from $\Delta\xi^2 = 1 \times 1\,\mathrm{mm}^2$ to $\Delta\xi^2 = 2 \times 2\,\mathrm{mm}^2$ would reduce (i.e. improve) RSP variance by a factor of 16, or RSP noise, i.e. $\sqrt{\mathrm{Var}_{\mathrm{RSP}}}$, by a factor of 4.

WEPL uncertainty (and consequently RSP uncertainty) due to TOF measurement error decreases as the object thickness increases, while the opposite is true for energy straggling (figure 3). For a ratio of TOF error over distance between sensor planes of 10-20 ps/m and a WEPL of 5 cm, both effects contribute to a similar extent (figure 4). For velocity errors $\sigma_t/L > 50\,\mathrm{ps/m}$, on the other hand, it is mainly the TOF measurement dominating the RSP resolution. Our results show that a 30 ps/m TOF system yields similar RSP resolution with a cylindrical object of 20 cm diameter as a 1% resolution calorimeter-based system (figure 5).

An additional source of image noise is multiple Coulomb scattering which depends on the shape and composition of the object. We estimated this contribution from the Monte Carlo simulated data. Our results show that RSP noise due to multiple Coulomb scattering reaches up to 0.4 % close to the water cylinder edge compared to 0.8 and 1.1 % due to straggling, TOF error, and beam spread for velocity errors of 30 ps and 50 ps, respectively. This is in good agreement with the results in (Dickmann et al., 2019, figure 7) who have studied the contribution of multiple Coulomb scattering to image noise in a calorimeter-based proton CT prototype (Johnson et al., 2016; Bashkirov et al., 2016) via Monte Carlo simulations. In heterogeneous regions of a patient head, i.e. including bone structures, nasal cavities, etc., the author's finding indicate that noise due to multiple Coulomb scattering becomes almost as important as noise due to the straggling, energy detection, and beam spread, and that it is present anywhere in the reconstructed image slice, including the centre. Since noise due to multiple Coulomb scattering is independent of the energy detection technique, we expect that TOF proton CT images of heterogeneous patient geometries will also be noisier than those of the homogeneous water cylinder presented here. We mention for completeness that Collins-Fekete et al. (2021) have also studied noise in proton CT images and found a non-negligible contribution of multiple Coulomb scattering, but their results are difficult to compare directly with ours as they mainly work in the projection domain and do not reconstruct noise images.

Worstell et al. (2019) presented a TOF proton CT prototype employing Large Area Picosecond Photon Detectors with a one sigma TOF error of 64 ps. In the setting used in this work, i.e. a water cylinder of 20 cm diameter, a dose to the centre of 10 mGy, and $1 \times 1\,\mathrm{mm}^2$ pixels, these detectors are expected to yield similar RSP resolution as a 2% calorimeter-based proton CT system (figure 5) if the TOF sensors are placed 1 m apart from each other. With a spacing of $L = 10\,\mathrm{cm}$, as reported in Worstell et al. (2019), the uncertainty on the exit energy due to the TOF measurement error would increase by a factor of ten (equation 2) and the RSP noise would range from about 4% at the centre to 13% at the cylinder edge for a beam energy of 200 MeV. Keeping the spacing at 10 cm, but reducing the incident beam energy to 180 MeV, which corresponds to a range in water of 21.6 cm, the RSP noise at the cylinder centre would reduce to 0.9% and to 9% near the edge. Vignati et al. (2020) performed first tests in a therapeutic proton beam with a new ultra fast silicon detector based on low gain avalanche diode (LGAD) technology (Pellegrini et al., 2014). They report a time resolution per sensor plane of 75 ps to 115 ps, i.e. TOF errors of 106 ps to 162 ps. Sadrozinski et al. (2018) had previously found TOF resolutions of an LGAD sensor of around 30 ps. Curtoni et al. (2021) studied the performance of Chemical Vapor Deposition diamond detectors in the context of ion beam therapy monitoring and reported time resolutions on the order of 100-200 ps between two sensor planes for protons depending on the energy, and as low as 13 ps for carbon ions. As the time resolution of these sensors depends on the particle's stopping power, it would benefit from an as low as possible residual energy. Based on our results, some of these new sensor types could be suitable for TOF proton CT in terms of time resolution.

In general, it would be crucial to devise an acquisition procedure which leads to an exit

energy as low as possible (figure 3 left). On the other hand, a lower incident beam energy also leads to stronger multiple Coulomb scattering and thus more noise due to multiple Coulomb scattering. Overall, the dependence of WEPL uncertainty on WEPL leads to a spatially varying RSP resolution in the reconstructed proton CT image. In particular, TOF proton CT images are expected to be noisier towards the object's edges than at its centre. This effect is not specific to TOF proton CT, however, but can also be seen in calorimeter-based proton CT (Rädler et al., 2018; Dickmann et al., 2019), where e.g. the energy measurement error in a scintillator varies as a function of deposited energy. Bashkirov et al. (2016) studied this aspect and proposed a multilayer scintillator system in order to make WEPL uncertainty less dependent on WEPL. The design of a TOF proton CT system will likely require a similar kind of study to achieve homogeneous image noise. Possible ways to adjust the noise distribution include energy degraders in front of the TOF system to reduce the residual energy, adapting the beam energy to the local phantom thickness (Dickmann et al., 2021), or modulating the beam fluence (Dickmann et al., 2020). Furthermore, given that the RSP resolution depends on the velocity error $\sigma_t/L$, designing a TOF proton CT will also require engineering efforts to integrate into a treatment room a system with a large distance between the sensor planes.

Although we concentrated on TOF proton CT in this work, we also provide a comparison with TOF helium CT in the appendix. We find that at equal residual range, equal fluence, and equal TOF measurement error, TOF helium CT is expected to yield about 30% lower RSP noise than TOF proton CT, which is due to reduced straggling and multiple Coulomb scattering. Note that both effects are independent of the energy detection method. Assuming the TOF measurement error to be lower by a factor of four with helium, RSP noise in TOF helium CT is close to the intrinsic limit due to straggling and beam spread for the considered cases $\sigma_t = 30\,\text{ps}$ and $\sigma_t = 50\,\text{ps}$. A comprehensive comparison of TOF-based helium and proton CT would require more details about the TOF sensor and properties of the TOF signal, including the impact of nuclear interactions and projectile fragmentation. At equal imaging dose, RSP noise in TOF helium CT is expected to be higher and would possibly be more comparable to that of TOF proton CT. A full dosimetric comparison of helium and proton CT was beyond the scope of this work. We point to (Collins-Fekete et al., 2021) for a more detailed analysis of the different ion species in ion CT.

As the purpose of this work was to characterise a proton CT modality, we have only considered direct reconstruction algorithms, and in particular the distance driven method described in Rit et al. (2013). Other direct methods exist, but have been shown to yield very similar results in terms of image noise and spatial resolution (Khellaf et al., 2020). We have not considered iterative reconstruction methods because image properties strongly depend on the parameters of the reconstruction, such as regularisation weights (Penfold et al., 2010; Penfold et al., 2015).

## 5 Conclusion

The purpose of this work was to investigate the RSP resolution, visible as image noise, in proton CT if TOF is used as energy measurement mechanism. The three noise contributions we considered were the TOF measurement error in relation to the spacing between the TOF sensor planes, the energy straggling experienced by the protons inside the scanned objects, as well as the proton beam's energy spread. For comparison, we also considered a calorimeter-based set-up which has been implemented in prototype scanners. Which of the three contributions dominates depends on the combination of beam energy and object thickness. For objects of up to 20 cm and a beam energy of 200 MeV, we find that beam spread and straggling are similarly relevant as the measurement error for velocity errors in the range of 10-50 ps/m. In TOF proton CT systems with a distance between the sensor planes of one metre and a time resolution of 100 ps or larger, the measurement error tends to be the most dominant source of RSP uncertainty unless the beam energy is chosen such that the exit energy is very low ($<$80 MeV). TOF proton CT

images of a 20 cm diameter water cylinder acquired at 10 mGy total dose to the object centre and reconstructed with a pixel size of 1 mm$^2$ have an RSP resolution of 1% or better when the velocity error is 50 ps/m or lower. We compared our model-based noise reconstructions with Monte Carlo simulated data and found a good agreement. The contribution to image noise due to multiple Coulomb scattering, which we estimated from the Monte Carlo data, was in itself consistent and comparable to previously reported results. RSP noise due to multiple Coulomb scattering was up to about 30% of the total RSP noise, depending on the location in the image and is expected to become more important in heterogeneous objects. RSP noise varies spatially in a TOF proton CT image and generally increases towards the object's edges. This is similar to, but more pronounced than, previously reported results for calorimeter-based proton CT systems. A calorimeter-based system with 1% energy error is comparable to a TOF-based system with a velocity error of 30 ps/m, and a 2% calorimeter system corresponds to a 64 ps/m TOF system. We compared RSP resolution in TOF proton CT and TOF helium, at equal residual range, and found that helium ions might offer better RSP resolution at equal fluence because of reduced straggling and multiple Coulomb scattering, but this advantage would be reduced at equal imaging dose. Overall, we expect that better resolution and more homogeneous image noise can be achieved by optimally adapting the beam energy to the phantom's water equivalent thickness.

## Acknowledgements

The work of Nils Krah was supported by ITMO-Cancer (CLaRyS-UFT project). This work was performed within the framework of the LABEX PRIMES (ANR-11-LABX-0063) of Université de Lyon.

## Appendix: Comparison with helium ion CT

In the following, we provide a short comparison with TOF helium CT and an estimate of the noise expected with that ion species. As starting point, we observe that the helium stopping power is about four times that of protons (because the particle charge squared appears in the Bethe Bloch equation) at four times the protons' kinetic energy. An incident helium beam must therefore have four times the kinetic energy of an incident proton beam to result in the same residual range downstream of an object. We compare TOF proton and helium CT at equal residual range and thus assume henceforth that kinetic energies are larger by a factor four.

We first consider the energy uncertainty $\sigma_{E_{\text{out}},\text{TOF}}$ due to the TOF measurement (equation 2). With $E_{\text{out,He}} \approx 4E_{\text{out},p}$ and $m_{\text{He}} \approx 4m_{\text{p}}$, and assuming the same TOF measurement error $\sigma_t$ for both ion species, one has

$$\begin{aligned}\sigma^2_{E_{\text{out}},\text{TOF,He}}(E_{\text{out,He}}) &= \frac{1}{m^4_{\text{He}}c^6}(E^2_{\text{out,He}} + 2m_{\text{He}}c^2E_{\text{out,He}})^3\ \frac{\sigma^2_{t,\text{He}}}{L^2} \\ &= \frac{1}{16^2m^4_{\text{p}}c^6}(16E^2_{\text{out},p} + 16\times 2m_{\text{p}}c^2E_{\text{out},p})^3\ \frac{\sigma^2_{t,\text{He}}}{\sigma^2_{t,\text{p}}}\frac{\sigma^2_{t,\text{p}}}{L^2} = 16\frac{\sigma^2_{t,\text{He}}}{\sigma^2_{t,\text{p}}}\sigma^2_{E_{\text{out}},\text{TOF,p}}(E_{\text{out,p}}). \quad (19)\end{aligned}$$

Concerning the energy uncertainty due to straggling (equation 3), we observe that the variable which depends on the choice of primary particle (proton or helium) is $\beta^2$, for which we find

$$\beta^2_{\text{He}} = \frac{E^2_{\text{He}} + 2m_{\text{He}}c^2E_{\text{He}}}{(E_{\text{He}} + m_{\text{He}}c^2)^2} = \frac{16}{16}\frac{E^2_{\text{p}} + 2m_{\text{He}}c^2E_{\text{p}}}{(E_{\text{p}} + m_{\text{He}}c^2)^2} = \beta^2_{\text{p}} \quad \text{with} \quad E_{\text{He}} \approx 4E_p \quad (20)$$

and consequently

$$\chi_{1,\text{He}}(E_{\text{He}})/K_{\text{He}} = \chi_{1,\text{p}}(E_{\text{p}})/K_{\text{p}} \quad \text{and} \quad \chi_{2,\text{He}}(E_{\text{He}})/K_{\text{He}} = \chi_{2,\text{p}}(E_{\text{p}})/K_{\text{p}}. \quad (21)$$

The pre-factor $K$ depends on the ion species (e.g. because it includes the particle charge), but since both functions, $\chi_1(E)$ and $\chi_2(E)$, contain the factor $K$, it simply cancels out in the integral expression (equation 3).

We therefore have

$$\sigma^2_{E_{\text{out}},\text{strag},\text{He}}(E_{\text{out,He}}) = \chi^2_{1,\text{He}}(E_{\text{out,He}}) \int_{E_{\text{out,He}}}^{E_{\text{in,He}}} \frac{\chi_{2,\text{He}}(E)}{\chi^3_{1,\text{He}}(E)}\,\mathrm{d}E \tag{22}$$

$$= 4\chi^2_{1,\text{p}}(E_{\text{out,p}}) \int_{E_{\text{out,He}}/4}^{E_{\text{in,He}}/4} \frac{\chi_{2,\text{He}}(4E')}{\chi^3_{1,\text{He}}(4E')}\,\mathrm{d}E' \tag{23}$$

$$= 4\chi^2_{1,\text{p}}(E_{\text{out,p}}) \int_{E_{\text{out,p}}}^{E_{\text{in,p}}} \frac{\chi_{2,\text{p}}(E')}{\chi^3_{1,\text{p}}(E')}\,\mathrm{d}E' \tag{24}$$

$$= 4\sigma^2_{E_{\text{out}},\text{strag,p}}(E_{\text{out,p}}), \tag{25}$$

where we have used the substitution $E \equiv 4E'$ from equation 22 to 23.

As stated earlier, the helium stopping power at $E_{\text{He}} = 4E_{\text{p}}$ is about 4 times greater than that of protons, i.e.

$$S^2_{\text{w,He}}(E_{\text{out,He}}) = 16 S^2_{\text{w,p}}(E_{\text{out,p}}). \tag{26}$$

With the above considerations, at $E_{\text{out,He}} = 4E_{\text{out,p}}$ and $E_{\text{in,He}} = 4E_{\text{in,p}}$, we find for the WEPL error due to straggling, energy detection and beam spread (equation 8):

$$\sigma^2_{\text{WEPL,He}} = \frac{\sigma^2_{E_{\text{out}},\text{strag,He}} + \sigma^2_{E_{\text{out}},\text{TOF,He}} + (\delta E_{\text{beam,He}} E_{\text{in,He}})^2}{S^2_{\text{w,He}} \Phi \Delta\xi^2}$$

$$= \frac{4\sigma^2_{E_{\text{out}},\text{strag,p}} + 16\frac{\sigma^2_{t,\text{He}}}{\sigma^2_{t,\text{p}}}\sigma^2_{E_{\text{out}},\text{TOF,p}} + 16(\delta E_{\text{beam,He}} E_{\text{in,p}})^2}{16 S^2_{\text{w,p}} \Phi \Delta\xi^2}$$

$$= \frac{\frac{1}{4}\sigma^2_{E_{\text{out}},\text{strag,p}} + \frac{\sigma^2_{t,\text{He}}}{\sigma^2_{t,\text{p}}}\sigma^2_{E_{\text{out}},\text{TOF,p}} + (\delta E_{\text{beam,He}} E_{\text{in,p}})^2}{S^2_{\text{w,p}} \Phi \Delta\xi^2}. \tag{27}$$

Concerning noise due to multiple Coulomb scattering, we observe that, within the multiple Coulomb scattering model by Lynch et al. (1991), the standard deviation of the angular and spatial distribution due to multiple Coulomb scattering scale with $z^2/\beta^2 p^2$, where $p$ is the particles' average momentum and $z$ their charge. Comparing helium ions and protons at $E_{\text{He}} = 4E_{\text{p}}$, we find

$$\left(\frac{z^2}{\beta^2 p^2}\right)_{\text{He}} = z^2_{\text{He}} \frac{(E_{\text{He}} + m_{\text{He}}c^2)^2 c^2}{(E_{\text{He}} + 2m_{\text{He}}c^2)^2 E^2_{\text{He}}} = \frac{4}{16}\frac{(E_{\text{p}} + m_{\text{p}}c^2)^2 c^2}{(E_{\text{p}} + 2m_{\text{p}}c^2)^2 E^2_{\text{p}}} = \frac{1}{4}\left(\frac{z^2}{\beta^2 p^2}\right)_{\text{p}}. \tag{28}$$

Therefore, at equal particle fluence, we expect the RSP variance due to multiple Coulomb scattering to be smaller by about a factor of 4 (or a factor of 2 in terms of RSP noise) for helium ions compared to protons. We also refer to (Collins-Fekete et al., 2016) for a more detailed comparison of helium ions and protons in the context of multiple Coulomb scattering and most likely path estimation.

Based on the above considerations, we conclude that at equal residual range and equal particle fluence $\Phi$, the helium RSP resolution intrinsically differs from that of protons by the straggling and multiple Coulomb scattering contributions. To which extent the TOF measurement plays a role depends on the ratio of TOF errors, $\sigma^2_{t,\text{He}}/\sigma^2_{t,\text{p}}$. If we assume a fixed TOF resolution independent of the ion species, i.e. $\sigma^2_{t,\text{He}}/\sigma^2_{t,\text{p}} = 1$, there is no difference in RSP resolution

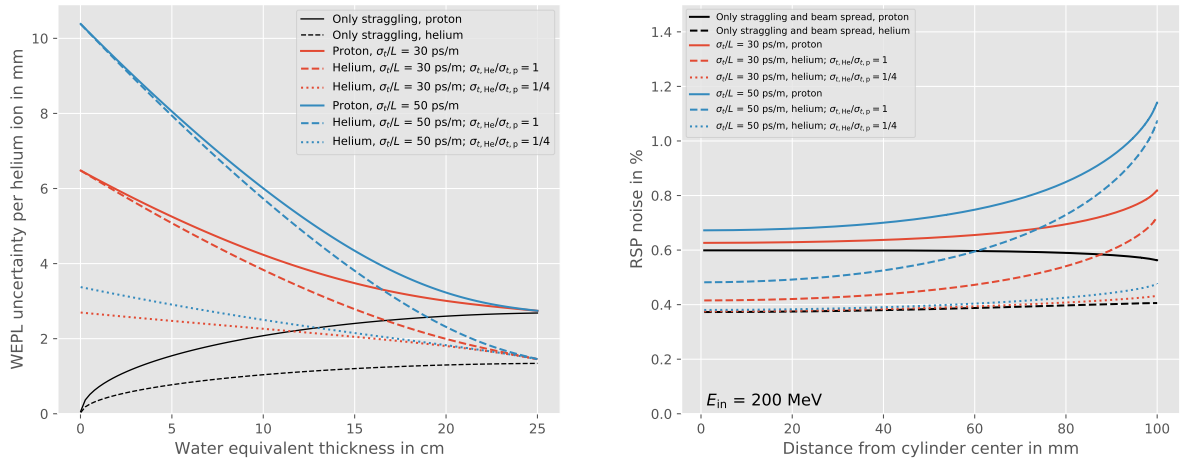


Figure 7: Left: Comparison of the expected WEPL error when using helium ions as opposed to protons. The comparison was done at equal residual range, i.e. at an incident proton beam energy of 200 MeV and an incident helium beam energy of 800 MeV. Right: Radial profiles of the RSP noise in reconstructed proton and helium CT images at equal particle fluence and equal residual range.

between helium and proton CT due to TOF measurement. In reality, however, the timing resolution of a detector depends on the signal strength which is generally four times greater with helium ions than with protons because of the four times higher stopping power of helium. If we assume $\sigma^2_{t,\mathrm{He}}/\sigma^2_{t,\mathrm{p}} = 1/4^2 = 1/16$, the contribution of $\sigma^2_{E_{\mathrm{out}},\mathrm{TOF},\mathrm{He}}(E_{\mathrm{out,He}})$ to the WEPL variance (equation 27) reduces by a factor of 16.

Finally, it needs to be acknowledged that dose to the patient is different for protons and helium ions. To derive a figure of merit relation, we consider that the dose due to protons absorbed by patient can be described as (Schulte et al., 2005)

$$D(E) = \frac{\Phi}{\rho}\left(S(E) + \kappa\gamma E\right), \tag{29}$$

where $S$ is the stopping power and the second term is the contribution of nuclear interactions. Assuming that a similar law holds for helium ions and considering that $S_{\mathrm{He}}(E_{\mathrm{He}}) = 4S_{\mathrm{p}}(E_{\mathrm{p}})$ and $E_{\mathrm{He}} = 4E_{\mathrm{p}}$, it is reasonable to suppose that imaging dose is about four times higher with helium ions than with protons. This implies that the fluence $\Phi$ would need to be four times lower in helium CT than in proton CT (at equal residual range) to achieve a comparable imaging dose, which in turn would increase the WEPL and RSP variance by a factor of 4 and the RSP noise by a factor of 2. A more rigorous treatment would need to consider the nuclear interactions and fragmentation of helium ions, but that would go beyond the scope of this work.

The left panel of figure 7 shows the expected WEPL error per particle in a TOF helium CT projection compared to TOF proton CT at equal residual range, based on the considerations and expressions derived above. We used the same absolute energy spread of the incident beam of 1 MeV for both, proton and helium, but we remark that this parameter depends on the accelerator. Noise due to multiple Coulomb scattering is not included but expected to be lower with helium ions. For an object whose thickness is close to the range of the particle beam, the WEPL error is lower by a factor of 2 for helium ions because of the reduced straggling. For thin objects where the TOF velocity error dominates we expect the same WEPL uncertainty for both ion types if we assume the same TOF error ($\sigma_{t,\mathrm{He}}/\sigma_{t,\mathrm{p}} = 1$) and a factor 2-2.5 lower uncertainty for helium if we assume a factor four lower TOF error ($\sigma_{t,\mathrm{He}}/\sigma_{t,\mathrm{p}} = 1/4$). The right panel of figure 7 shows the RSP noise to be expected in a reconstructed image of the water cylinder for protons (solid) and helium ions (dashed and dotted) at equal particle fluence and equal residual

range, i.e. an incident proton beam energy of 200 MeV and an incident helium beam energy of 800 MeV. The effect of multiple Coulomb scattering is not included. For equal TOF measurement error, $\sigma_{t,\mathrm{He}}/\sigma_{t,\mathrm{p}} = 1$, the RSP resolution in TOF helium CT is 20-30% better with helium ions than with protons. Assuming a four times smaller TOF uncertainty, $\sigma_{t,\mathrm{He}}/\sigma_{t,\mathrm{p}} = 1/4$, the RSP noise is a factor two smaller with helium ions than with protons.

## References


A. Kak et al. (2001). "3. Algorithms for Reconstruction with Nondiffracting Sources". In: *Principles of Computerized Tomographic Imaging*. Society for Industrial and Applied Mathematics, pp. 49–112. DOI: 10.1137/1.9780898719277.ch3.

Agostinelli, S. et al. (2003). "GEANT4 - A simulation toolkit". In: *Nuclear Instruments and Methods in Physics Research, Section A: Accelerators, Spectrometers, Detectors and Associated Equipment* 506.3, pp. 250–303. ISSN: 01689002. DOI: 10.1016/S0168-9002(03)01368-8.

Alme, J. et al. (2020). "A High-Granularity Digital Tracking Calorimeter Optimized for Proton CT". In: *Frontiers in Physics* 8. ISSN: 2296-424X. DOI: 10.3389/fphy.2020.568243.

Bashkirov, V. A. et al. (2016). "Novel scintillation detector design and performance for proton radiography and computed tomography". In: *Medical Physics* 43.2, pp. 664–674. ISSN: 00942405. DOI: 10.1118/1.4939255.

Berger, M. J. et al. (1993). "Report 49". In: *Journal of the International Commission on Radiation Units and Measurements* os25.2. ISSN: 1742-3422. DOI: 10.1093/jicru/os25.2.Report49.

Berger, M. et al. (2005). *ESTAR, PSTAR, and ASTAR: Computer Programs for Calculating Stopping-Power and Range Tables for Electrons, Protons, and Helium Ions (version 1.2.3)*. DOI: 10.18434/T4NC7P.

Civinini, C. et al. (2013). "Recent results on the development of a proton computed tomography system". In: *Nuclear Instruments and Methods in Physics Research, Section A: Accelerators, Spectrometers, Detectors and Associated Equipment* 732, pp. 573–576. ISSN: 01689002. DOI: 10.1016/j.nima.2013.05.147.

Collins-Fekete, C.-A. et al. (2016). "A theoretical framework to predict the most likely ion path in particle imaging". In: *Physics in Medicine & Biology* 62.October, pp. 1777–1790.

Collins-Fekete, C.-A. et al. (2021). "Statistical limitations in ion imaging". In: *Physics in Medicine & Biology* 66.10, p. 105009. ISSN: 0031-9155. DOI: 10.1088/1361-6560/abee57.

Curtoni, S. et al. (2021). "Performance of CVD diamond detectors for single ion beam-tagging applications in hadrontherapy monitoring". In: *Nuclear Instruments and Methods in Physics Research Section A: Accelerators, Spectrometers, Detectors and Associated Equipment* 1015, p. 165757. ISSN: 01689002. DOI: 10.1016/j.nima.2021.165757.

DeJongh, E. A. et al. (2021). "Technical Note: A fast and monolithic prototype clinical proton radiography system optimized for pencil beam scanning". In: *Medical Physics* 48.3, pp. 1356–1364. ISSN: 0094-2405. DOI: 10.1002/mp.14700.

Dickmann, J. et al. (2020). "An optimization algorithm for dose reduction with fluenceâĂŞmodulated proton CT". In: *Medical Physics*, mp.14084. ISSN: 0094-2405. DOI: 10.1002/mp.14084.

Dickmann, J. et al. (2019). "Prediction of image noise contributions in proton computed tomography and comparison to measurements". In: *Physics in Medicine & Biology* 64.14, p. 145016. ISSN: 1361-6560. DOI: 10.1088/1361-6560/ab2474.

Dickmann, J. et al. (2021). "Proof of concept image artifact reduction by energy-modulated proton computed tomography (EMpCT)". In: *Physica Medica* 81, pp. 237–244. ISSN: 11201797. DOI: 10.1016/j.ejmp.2020.12.012.

Feldkamp, L. a. et al. (1984). "Practical cone-beam algorithm". In: *Journal of the Optical Society of America A* 1.6, p. 612. ISSN: 1084-7529. DOI: 10.1364/JOSAA.1.000612.

Johnson, R. P. et al. (2016). "A Fast Experimental Scanner for Proton CT: Technical Performance and First Experience With Phantom Scans". In: *IEEE Transactions on Nuclear Science* 63.1, pp. 52–60. ISSN: 0018-9499 VO - 63. DOI: 10.1109/TNS.2015.2491918.

Johnson, R. P. (2018). "Review of medical radiography and tomography with proton beams". In: *Reports on Progress in Physics* 81.1, p. 016701. ISSN: 0034-4885. DOI: 10.1088/1361-6633/aa8b1d.

Khellaf, F. et al. (2020). "A comparison of direct reconstruction algorithms in proton computed tomography". In: *Physics in Medicine & Biology* 65.10, p. 105010. ISSN: 1361-6560. DOI: 10.1088/1361-6560/ab7d53.

Krah, N. et al. (2020). "Scattering proton CT". In: *Physics in Medicine & Biology* 65.22, p. 225015. ISSN: 1361-6560. DOI: 10.1088/1361-6560/abbd18.

Lynch, G. R. et al. (1991). "Approximations to multiple Coulomb scattering". In: *Nuclear Instruments and Methods in Physics Research Section B: Beam Interactions with Materials and Atoms* 58.1, pp. 6–10. ISSN: 0168583X. DOI: 10.1016/0168-583X(91)95671-Y.

Paganetti, H. (2012). *Proton Therapy Physics*. Ed. by H. Paganetti. Boca Raton: Taylor & Francis Group. ISBN: 9781439836453.

Payne, M. G. (1969). "Energy Straggling of Heavy Charged Particles in Thick Absorbers". In: *Physical Review* 185.2, pp. 611–623. ISSN: 0031-899X. DOI: 10.1103/PhysRev.185.611.

Pellegrini, G. et al. (2014). "Technology developments and first measurements of Low Gain Avalanche Detectors (LGAD) for high energy physics applications". In: *Nuclear Instruments and Methods in Physics Research Section A: Accelerators, Spectrometers, Detectors and Associated Equipment* 765, pp. 12–16. ISSN: 01689002. DOI: 10.1016/j.nima.2014.06.008.

Pemler, P et al. (1999). "A detector system for proton radiography on the gantry of the Paul-Scherrer-Institute". In: *Nuclear Instruments and Methods in Physics Research Section A: Accelerators, Spectrometers, Detectors and Associated Equipment* 432.2-3, pp. 483–495. ISSN: 0168-9002. DOI: DOI:10.1016/S0168-9002(99)00284-3.

Penfold, S. N. et al. (2010). "Total variation superiorization schemes in proton computed tomography image reconstruction." In: *Medical physics* 37.11, pp. 5887–5895. ISSN: 00942405. DOI: 10.1118/1.3504603.

Penfold, S. et al. (2015). "Techniques in Iterative Proton CT Image Reconstruction". In: *Sensing and Imaging* 16.1, p. 19. ISSN: 1557-2064. DOI: 10.1007/s11220-015-0122-3.

Quiñones, C. T. et al. (2016). "Filtered back-projection reconstruction for attenuation proton CT along most likely paths". In: *Physics in Medicine and Biology* 61.9, pp. 3258–3278. ISSN: 0031-9155. DOI: 10.1088/0031-9155/61/9/3258.

Rädler, M. et al. (2018). "Two-dimensional noise reconstruction in proton computed tomography using distance-driven filtered back-projection of simulated projections". In: *Physics in Medicine & Biology* 63.21, p. 215009. ISSN: 1361-6560. DOI: 10.1088/1361-6560/aae5c9.

Ramachandran, G. N. et al. (1971). "Three-dimensional Reconstruction from Radiographs and Electron Micrographs: Application of Convolutions instead of Fourier Transforms". In: *Proceedings of the National Academy of Sciences* 68.9, pp. 2236–2240. ISSN: 0027-8424. DOI: 10.1073/pnas.68.9.2236.

Rit, S. et al. (2013). "Filtered backprojection proton CT reconstruction along most likely paths." In: *Medical physics* 40.3, p. 031103. ISSN: 0094-2405. DOI: 10.1118/1.4789589.

Sadrozinski, H. F.-W. et al. (2018). "4D tracking with ultra-fast silicon detectors". In: *Reports on Progress in Physics* 81.2, p. 026101. ISSN: 0034-4885. DOI: 10.1088/1361-6633/aa94d3.

Sarrut, D. et al. (2014). "A review of the use and potential of the GATE Monte Carlo simulation code for radiation therapy and dosimetry applications". In: *Medical Physics* 41.6Part1, p. 064301. ISSN: 00942405. DOI: 10.1118/1.4871617.

Schippers, J. M. (2018). "Beam Transport Systems for Particle Therapy". In: *Proceedings of the CAS-CERN Accelerator School: Accelerators for Medical Applications,* ed. by R. Bailey. Vösendorf, Austria: CERN. DOI: 10.23730/CYRSP-2017-001.241.

Schulte, R. W. et al. (2008). "A maximum likelihood proton path formalism for application in proton computed tomography". In: *Medical Physics* 35.11, p. 4849. ISSN: 00942405. DOI: 10.1118/1.2986139.

Schulte, R. W. et al. (2005). "Density resolution of proton computed tomography". In: *Medical Physics* 32.4, pp. 1035–1046. ISSN: 00942405. DOI: 10.1118/1.1884906.

Taylor, J. T. et al. (2016). "An experimental demonstration of a new type of proton computed tomography using a novel silicon tracking detector". In: *Medical Physics* 43.11, pp. 6129–6136. ISSN: 00942405. DOI: 10.1118/1.4965809.

Tschalär, C. (1968). "Straggling distributions of large energy losses". In: *Nuclear Instruments and Methods* 61.2, pp. 141–156. ISSN: 0029554X. DOI: 10.1016/0029-554X(68)90535-1.

Ulrich-Pur, F. et al. (2022). "Feasibility study of a proton CT system based on 4D-tracking and residual energy determination via time-of-flight". In: *Physics in Medicine & Biology* 67.9, p. 095005. ISSN: 0031-9155. DOI: 10.1088/1361-6560/ac628b.

Vignati, A et al. (2020). "A new detector for the beam energy measurement in proton therapy: a feasibility study". In: *Physics in Medicine & Biology* 65.21, p. 215030. ISSN: 1361-6560. DOI: 10.1088/1361-6560/abab58.

Volz, L. (2020). "Particle imaging for daily in-room image guidance in particle therapy". PhD thesis. University of Heidelberg, p. 281. DOI: 10.11588/heidok.00029273.

Worstell, W. A. et al. (2019). "First results developing time-of-flight proton radiography for proton therapy applications". In: *Medical Imaging 2019: Physics of Medical Imaging*. Ed. by H. Bosmans et al. SPIE, p. 15. ISBN: 9781510625433. DOI: 10.1117/12.2511804.

Wunderlich, A. et al. (2008). "Image covariance and lesion detectability in direct fan-beam x-ray computed tomography". In: *Physics in Medicine and Biology* 53.10, pp. 2471–2493. ISSN: 0031-9155. DOI: 10.1088/0031-9155/53/10/002.